Advanced functional safeguarding composites with enhanced anti-impact and excellent thermal properties
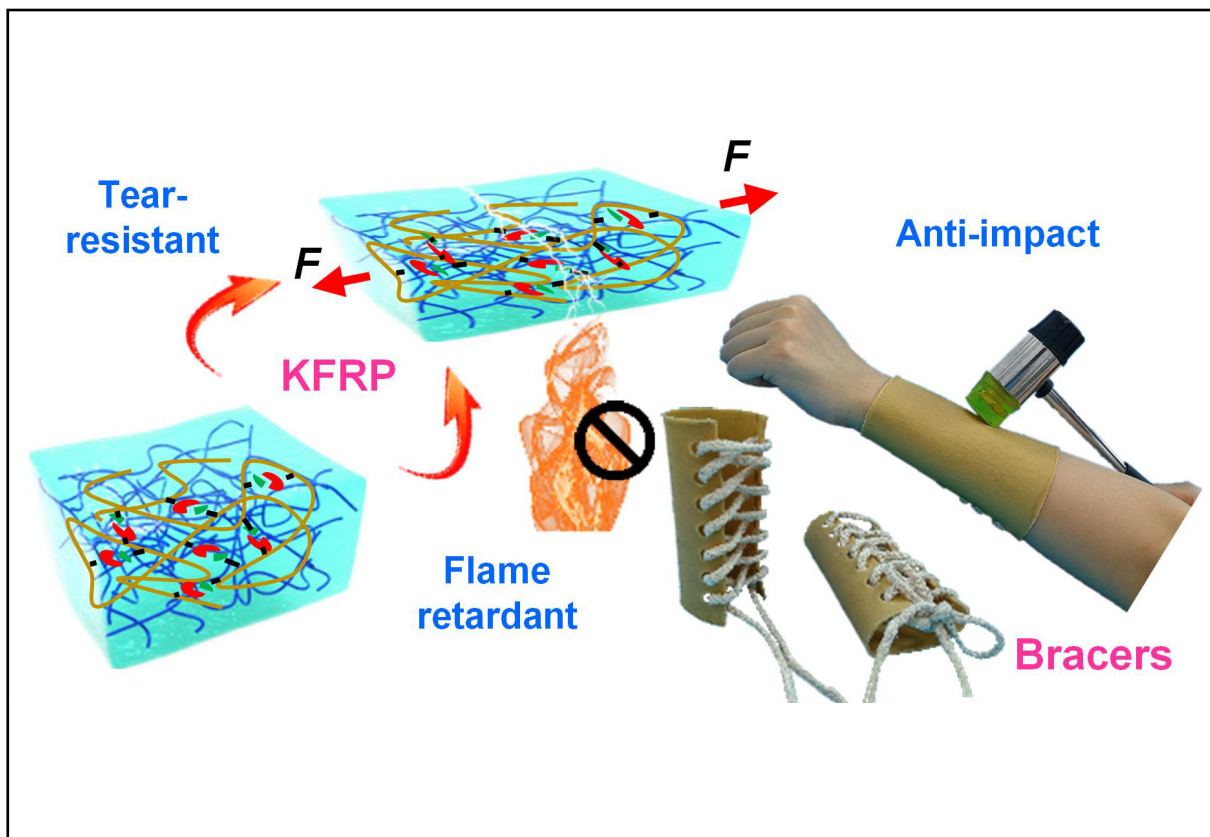
Wenhui Wang, Sheng Wang ✉, Shuai Liu, Jianyu Zhou, Junshuo Zhang, Fang Yuan, Min Sang, and Xinglong Gong ✉

CAS Key Laboratory of Mechanical Behavior and Design of Materials, Department of Modern Mechanics, University of Science and Technology of China, Hefei 230027, China

✉Correspondence: Sheng Wang, E-mail: wsh160@ustc.edu.cn; Xinglong Gong, E-mail: gongxl@ustc.edu.cn

Graphical abstract

Kevlar fiber reinforced polymers (KFRP) with tear-resistant and flame retardant properties were applied to safeguard bracers.

Public summary

■ Kevlar fiber reinforced polymers (KFRP) showed shear stiffening behavior and enhanced strength and toughness.

■ KFRP exhibited excellent anti-impact and stab-resistant performance.

■ KFRP presented improved heat transfer property and flame retardancy.

■ Functional bracers based on KFRP were successfully manufactured.

JUSTC⁺

Advanced functional safeguarding composites with enhanced anti-impact and excellent thermal properties

Wenhui Wang, Sheng Wang ✉, Shuai Liu, Jianyu Zhou, Junshuo Zhang, Fang Yuan, Min Sang, and Xinglong Gong ✉

CAS Key Laboratory of Mechanical Behavior and Design of Materials, Department of Modern Mechanics, University of Science and Technology of China, Hefei 230027, China

✉Correspondence: Sheng Wang, E-mail: wsh160@ustc.edu.cn; Xinglong Gong, E-mail: gongxl@ustc.edu.cn

Abstract: Personal safety protection has played an important role in daily life. Developing advanced functional safeguarding composites with enhanced anti-impact and excellent thermal properties will be a significant development for body armor. Herein, Kevlar fiber reinforced polymers (KFRP) were fabricated by introducing short Kevlar fibers (KFs) into a shear stiffening elastomer (SSE). The storage modulus of KFRP with 15 wt% KFs (KFRP-15%) increased from 222.8 kPa to 830.8 kPa when the shear frequency varied from 0.1 Hz to 100 Hz. KFRP-15% achieved a higher tensile strength (2.65 MPa) and fracture toughness (11.95 kJ/m²) than SSE in the vertical type, showing superior tear resistance. Additionally, KFRP-15% exhibited promising anti-impact properties, which could dissipate the drop hammer impact force from 1.74 kN to 0.56 kN and remained intact after 10 consecutive impacts. Moreover, KFRP-15% also presented excellent stab-resistant performance. In addition, KFRP-15% also showed improved heat transfer properties, flame retardancy, and smoke suppression capabilities. Finally, functional bracers based on KFRP-15% for protection, thermal-dissipation, and flame-retardant were successfully prepared.

Keywords: Kevlar; shear stiffening elastomer; fiber reinforced polymers; safeguarding; thermal properties

CLC number: TB332   **Document code:** A

1   Introduction

The human body is often injured during sports, natural disasters, and wars. The demand for high-performance safeguarding materials has become increasingly prominent in practical applications. However, conventional impact protection materials have not satisfied the requirements for complicated situations, for instance, heat transfer capability for wearing comfort and flame retardancy in fire[1–3]. The composite with improved thermal conductivity and flame retardancy was fabricated by forming a core-shell structured graphene oxide coating Al_2O_3 hybrid[4]. However, it did not present impact resistance and energy absorption. Therefore, developing wearable functional safeguarding composites is still a challenge.

Fiber reinforcement is one of the most effective approaches to functionalize various properties of traditional materials[5, 6]. Kevlar fiber (KF) is a kind of aramid fiber with high tensile strength (~3.6 GPa), high modulus (~90 GPa), low density (~1.44 g/cm³), and excellent thermal stability (degrading temperature >500 ℃)[7, 8]. It has been widely applied in composite materials, bulletproof products, and electrolyte membranes[9–11]. Accordingly, KF has been proven to be an ideal reinforcing filler to improve the mechanical properties of polymers. For instance, 10 wt% short Kevlar fibers were introduced to the polypropylene matrix, leading to an increase in tensile strength from 30 MPa to 47 MPa[12]. The modified Kevlar nanofibers were utilized to prepare styrene-

butadiene rubber composites, whose tensile strength and tear strength were increased by 576% and 202%, respectively[13]. In addition to reinforcing mechanical properties, introducing KFs into polymers also endowed them with other functionalities, such as thermal stability, protection performance, shielding, and flame-retardant capability[14–16]. For example, KFs were applied to crop straw-polyethylene composites, showing improved thermal stabilities and self-extinguishing capabilities[17]. Therefore, KF is an ideal candidate for reinforcing polymers.

Shear stiffening elastomer (SSE), as a typical smart composite, is generally regarded as an outstanding protective material due to its excellent energy dissipation and impact hardening effect[18]. For example, the SSE-based triboelectric nanogenerator (TENG) absorbed more kinetic energy than silicone rubber during accidental impact loading[19]. Generally, nanoparticles are introduced into SSEs to endow them with multi-functionality, such as carbonyl iron particles[20] and carbon nanotubes[21]. However, these nanoparticles did not significantly improve the mechanical properties of SSE. In particular, SSE was always severely damaged when subjected to a violent impact. An SSE-based sensor was destroyed by a 30 cm drop hammer impact[22]. Furthermore, the TENG fabricated by the shear stiffening hybrid elastomer with polytetrafluoroethylene nanoparticles also failed under the drop hammer impact of 40 cm[23]. Thus, although various composites and flexible devices based on SSE have been developed, their low tear strength and sharp-impact resistance have not

been effectively addressed. To improve their practical applicability and prevent the devices from being torn and damaged during use, it is extremely necessary to enhance the mechanical performance of SSEs.

Herein, Kevlar fiber reinforced polymers (KFRP) were successfully manufactured by introducing KFs into SSEs. KFRP showed excellent mechanical properties owing to the introduction of KFs. The tensile strength and toughness of KFRP were dramatically increased. Furthermore, the anti-impact and stab-resistant properties of KFRP were investigated by drop hammer impact tests and spike and knife punching experiments. In addition, a fracture morphology study was conducted to explore the failure mechanisms. Moreover, KFRP exhibited better thermal conduction, flame retardancy and smoke suppression abilities. Finally, KFRP were applied to functional wristbands.

2   Materials and methods

2.1   Materials

All chemical reagents were purchased from commercial sources and used without further purification. Hydroxyl silicone oil was supplied by Jining Huakai Resin Co., Ltd. Boric acid and benzoyl peroxide (BPO) were purchased from Sinopharm Chemical Reagent Co. Ltd. Methyl vinyl silicone rubber (VMQ) was provided by Shenzhen Muwei Technology Co., Ltd. Short KFs with a length of 3 mm were purchased from Dongguan Shengxin Special Strap Co., Ltd.

2.2   Manufacturing process

Boric acid was added to hydroxyl silicone oil with a mass ratio of 1 : 36. After thorough mixing, the solution was heated at 180 °C for 2 h. During the process, octanoic acid was also added. Then, by cooling the mixture to room temperature, the shear stiffening gel (SSG) was obtained.

Next, the prepared SSG and the VMQ at a mass ratio of 7 : 3 were mixed together by a double-roll mill (Taihu Rubber Machinery Inc., China, Model XK-160). The vulcanized agent of BPO was added. Subsequently, KFs were also mixed into the composites at different mass fractions. The final material was pressed into an aluminum mold and vulcanized at 100 °C and 20 MPa for 15 min to obtain the KFRP. When the mass ratio of Kevlar was X%, the composite was named KFRP-X%. KFRP-5%, KFRP-10% and KFRP-15% were prepared in this work.

2.3   Characterization

The surfaces and failure morphologies were observed by the digital optical microscope (KEYENCE VHX-200). The micromorphology of KFs was characterized by field emission scanning electron microscopy (SEM, Gemini 500, Carl Zeiss Jena, Germany). The rheological properties of KFRP were tested by a commercial rheometer (Physica MCR 302, Anton Paar Co., Austria) with a parallel plate (diameter of 20 mm). Tensile tests and crack propagation experiments were measured using a universal tensile instrument (MTS, CriterionTM Model 43). In the undeformed state, the length and thickness of unnotched KFRP used to measure the fracture toughness were 70 mm and 2 mm, respectively. The height between two

grippers was 20 mm. The precracked KFRP were prepared by cutting a crack of 15 mm with a blade. The digital image correlation (DIC) method was utilized to analyze the deformation of KFRP during the crack propagation[24, 25]. The anti-impact performance and stab resistance properties of the KFRP were investigated by a drop hammer test device. Thermal conductivity was measured by a thermal constants analyzer (Hot Disk TPS 2500 S). An infrared thermal imaging camera (TESTO 865) was used to record the infrared images. In addition, the complete burning experiments of KFRP were carried out by an FTT2000 cone calorimeter (CCT) at a heat flux of 35 kW/m^2 and a sample size of 100 mm × 100 mm × 3 mm under the ISO5660 standard.

3   Results and discussion

3.1   Preparation and characterization of the KFRP

The KFRP were fabricated by dispersing KFs into SSE (Fig. 1a). Due to large numbers of B–O bonds in SSE interacting with each other to impede the movement of polymer chains during impact, KFRP enabled the absorption and dissipation of much energy. The length of the KFs used was 3 mm, and the diameter was 12 μm (Fig. S1a). The surface morphologies of KFRP with different KF contents are shown in Fig. 1b and Fig. S1b. SSE was transparent. As the KFs increased, the color of the composites became yellow. In KFRP-5%, KFs were staggered and disorderly distributed. Interestingly, most of the fibers exhibited similar orientations in KFRP-10%, and this phenomenon was more obvious in KFRP-15%. This was attributed to KFs withstanding directional shear force by the double-roll mill during the mixing process. Similarly, the fiber distributions in the cross-section of KFRP displayed a layered characteristic. Simultaneously, some fibers intertwine along the thickness direction, which can enhance the stiffness of KFRP. Furthermore, the mechanical enhancement of KFs on the SSE was first confirmed in Fig. 1c. The composites were 120 mm × 120 mm × 2 mm. Notably, SSE was very soft and collapsed owing to self-weight. By comparison, the deformation of KFRP-5% was greatly reduced, while KFRP-10% could even support a weight of 20 g. In particular, KFRP-15% could maintain its original shape under 20 g loading. As a result, KFRP-15% exhibited the greatest flexural rigidity and excellent load-bearing capacity.

The rheological properties of the KFRP were investigated under the oscillatory shear mode when the shear rate was 0.1%. KFRPs presented a typical shear stiffening behavior, and their storage modulus (G') increased with shear frequency (Fig. 1d). The initial G' of SSE was 4.7 kPa, and it increased by 43 times (203.4 kPa) as soon as the shear frequency reached 100 Hz. Likewise, the G' of KFRP-15% increased from 222.8 kPa to 830.8 kPa, when the shear frequency varied from 0.1 Hz to 100 Hz. Undoubtedly, Kevlar fiber contents exhibited a positive influence on G'. Moreover, the G' of SSE was independent of shear strain. However, G' of KFRP decreased with increasing of shear strain when the shear frequency was 0.1 Hz. In particular, the Payne effect of KFRP-15% was more remarkable, which indicated that the microstructures of the composites were more sensitive to shear
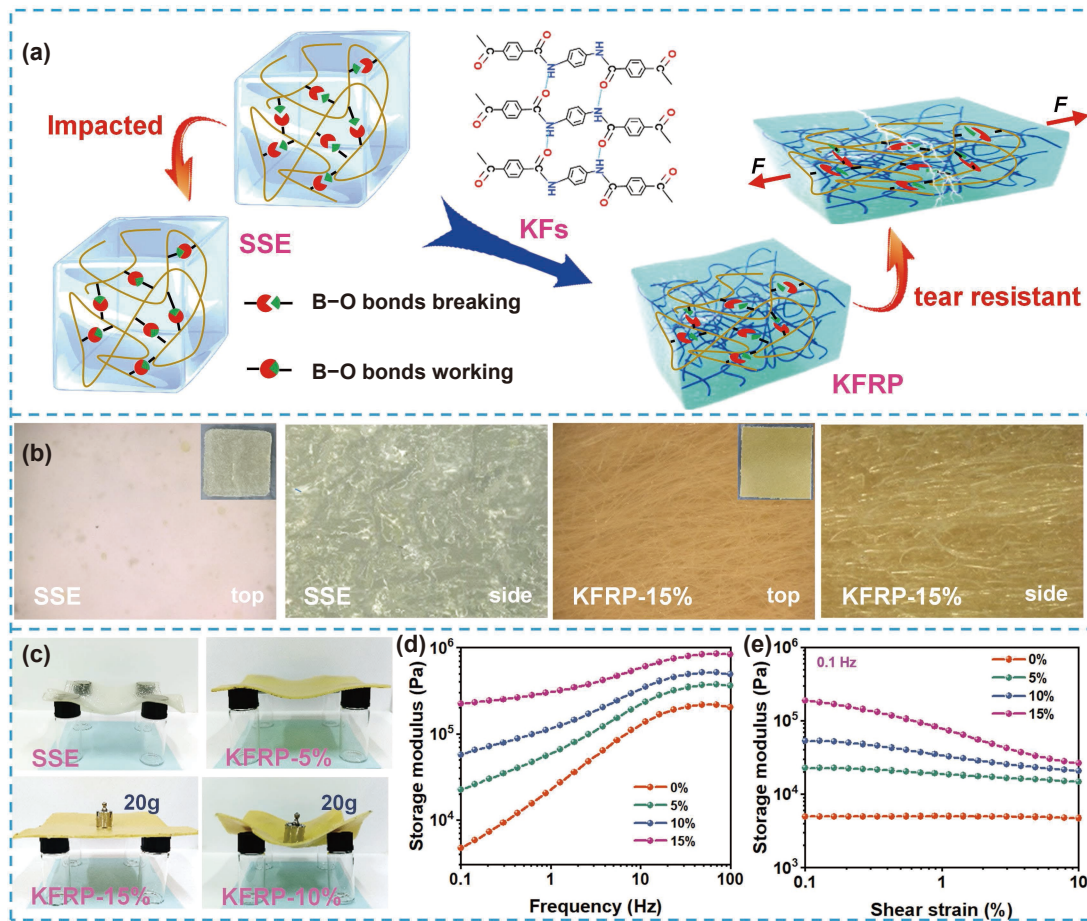
Fig. 1. (a) Illustration of the fabrication method for KFRPs. (b) The surface and cross-sectional morphology of SSE and KFRP-15%. (c) Photographs of the as-prepared KFRPs to bear loads. (d) Storage modulus vs. shear frequency of KFRPs when the shear strain was 0.1%. (e) The Payne effects of KFRPs.

strain (Fig. 1e)[26, 27]. Thus, the mechanical properties of the composites were significantly affected by the introduction of fibers.

3.2 Tensile and tear resistance of KFRP

Furthermore, uniaxial tensile tests were performed to investigate the reinforcing effect of the KFs in the KFRP. The composites with a size of 50 mm × 8 mm × 2 mm could be divided into two types according to the orientation of the fibers: vertical and horizontal (Fig. S2). Most fibers of the vertical type specimens were parallel to the tensile direction, while those of the horizontal types were perpendicular to the stretching force. The tensile stress-strain curves of KFRP in two ways are recorded in Fig. 2a, b. For SSE, they both showed linear elastic deformation in the initial stage and then fractured suddenly. However, the stretching process of KFRP could be divided into several stages, and the critical points/regions were marked. Region 1: stress increasing period, which exhibited a limited linear elastic behavior in an initial range followed by a nonlinear elastoplastic stage. Point a: tensile strength. Region 2: necking occurred, and the width decreased. Point b: crack formation and delamination initiation. Region 3: delamination propagation. Point c: fracture stress. Region 4: break occurred. Region 3 did not exist in the stress-strain curves of the horizontal type, indicating that the horizontal tensile KFRP did not undergo delamination failure.

This result could be further supported by the photographs of the destructive morphology after stretching (Fig. S2). Besides, after the horizontal KFRP was stretched, many fibers at the fracture turned around with the large deformation of the matrix, gradually paralleling the stretching direction. To further explore KFRP's nonlinear behavior, a coupled damage-plasticity model has been developed, which could be described by the combination of plastic strain accumulation and stiffness degradation (Fig. S3d). The fitting results were in good agreement with the experimental results as shown in Fig. S3e.

Additionally, the typical stretching process is shown in Fig. 2c. The breaking length of KFRP was several times longer than the original length. The tensile strengths showed an increasing trend with the increase in mass fraction of KFs (Fig. S3a and Table S2). The value of vertical tensile strength was higher than that of the horizontal type. For instance, the tensile strength of KFRP-15% at vertical type was 2.62 MPa, which was 2083.3% larger compared to SSE and 164.6% higher than the horizontal type. Moreover, the enclosed area obtained by integrating the stress-strain curve represented the tensile toughness of the composite material[28]. The tensile toughness of KFRP was also dramatically enhanced compared with that of SSE (Fig. S3b and Table S2). Overall, the mechanical properties of KFRP-15% were significantly enhanced. The rate-dependent tensile behavior of KFRP-15%
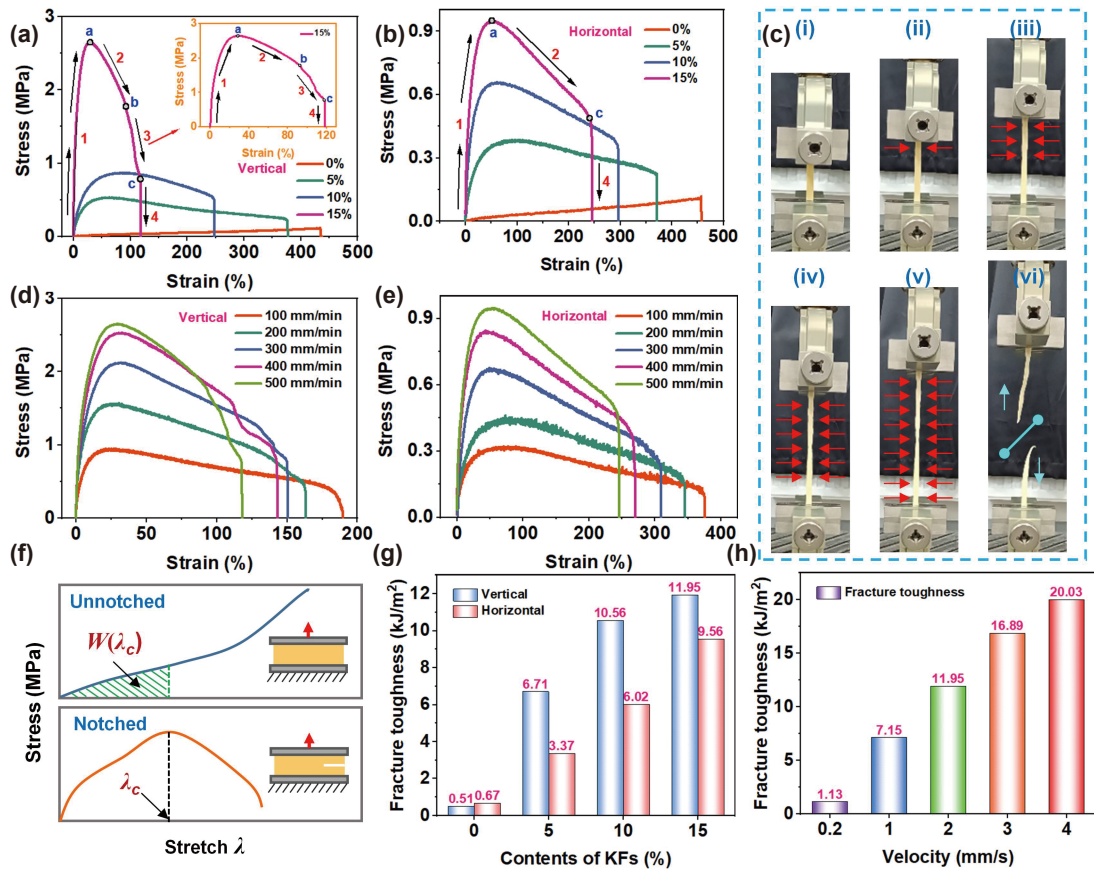
Fig. 2. Tensile stress-strain curves of KFRP whose fibers were (a) vertical and (b) horizontal at a speed of 500 mm/min. (c) The typical stretching process of KFRP-15%. The tensile stress-strain curves of KFRE-15% in the (d) vertical and (e) horizontal types at different tensile rates. (f) Definition of fracture toughness. (g) Fracture toughness of KFRP. (h) Fracture toughness of KFRP-15% with vertical fiber orientation at different tensile rates.

was also investigated. In Fig. 2d and e, there was a continual increase in tensile strength and a gradual decrease in elongation at break as the stretching rates increased, which was due to the shear stiffening effect of SSE. In the same way, the toughness of KFRP-15% at different tensile velocities is illustrated in Fig. S3c. The toughness values at high stretching rates were larger than those at low velocities, which was mainly because the tensile strength of KFRP-15% increased remarkably with the stretching speed, leading to fracture under higher stress.

Furthermore, crack propagation tests were carried out to evaluate the tear resistance of KFRP. Fracture toughness was measured using a two-sample method (Fig. 2f). The unnotched KFRP were used to measure the stress-stretch curve, and its enveloped area indicated the elastic energy density, $W(\lambda)$. The KFRP with the initial crack was used to measure the critical rupture stretch λc. Thus, the fracture toughness was calculated by $\Gamma c = W(\lambda c)H$, where H represented the height of composites. The increasing content of KFs resulted in the enhancement of stress and the decrement in λc (Fig. S4a and b). For instance, the stress of vertical KFRP-15% was 1.7 MPa at $\lambda c = 1.46$, while it decreased to 40.2 kPa at $\lambda c = 1.95$ for SSE. The stress of the horizontal KFRP increased from 39.2 kPa to 1.22 MPa when the Kevlar mass fraction varied from 0% to 15%. Additionally, λc of the horizontal type was higher than that of the vertical KFRP. The fracture toughness of KFRP also showed an upward trend with the increasing content of KFs (Fig. 2g and Table S2).

The fracture toughness of SSE was only 0.51 kJ/m², while the vertical Γc values of KFRP-5%, KFRP-10%, and KFRP-15% were significantly enhanced by 1215.7%, 1970.6%, and 2243.1%, respectively. The horizontal Γc of KFRP-15% was 9.56 kJ/m², which was 14.3 times as high as SSE.

Besides, the deformation morphologies and the Lagrange strain fields in the y-direction (ε_{yy}) of KFRP recorded by the CCD camera are shown in Fig. S4d. At the same elongation, the ε_{yy} of KFRP gradually decreased with the increasing mass fraction of KFs. At $\lambda=1.50$, ε_{yy} attained its maximum at the crack tip. As λ increased to 2.10, the SSE had already cracked, and the crack propagated rapidly. However, even when λ further increased to 2.12, the crack tip of KFRP-15% did not start to move due to the introduction of KFs, indicating that it can effectively limit propagation of the crack tip, further proving that KFRP-15% exhibited better tear resistance than SSE. In addition, when λ increased from 2.00 to 3.50, the KFRP-15% crack tip still propagated slowly and the crack tip velocity was approximately 0.41 mm/s (Fig. S5).

Moreover, the rate-dependent crack propagation behavior of KFRP-15% with vertical KF orientation was also studied. The tensile rate presented a positive influence on the stress and fracture toughness of KFRP-15% during crack propagation (Fig. S4c and Fig. 2h). When the stretch was 1.2, the stress of KFRP-15% was 0.31 MPa at a tensile speed of 0.2 mm/s, while it was 2.72 MPa at 4 mm/s. Additionally, the calculated fracture toughness of KFRP-15% increased from 1.13 kJ/m² to 20.03 kJ/m² when the tensile rate changed from
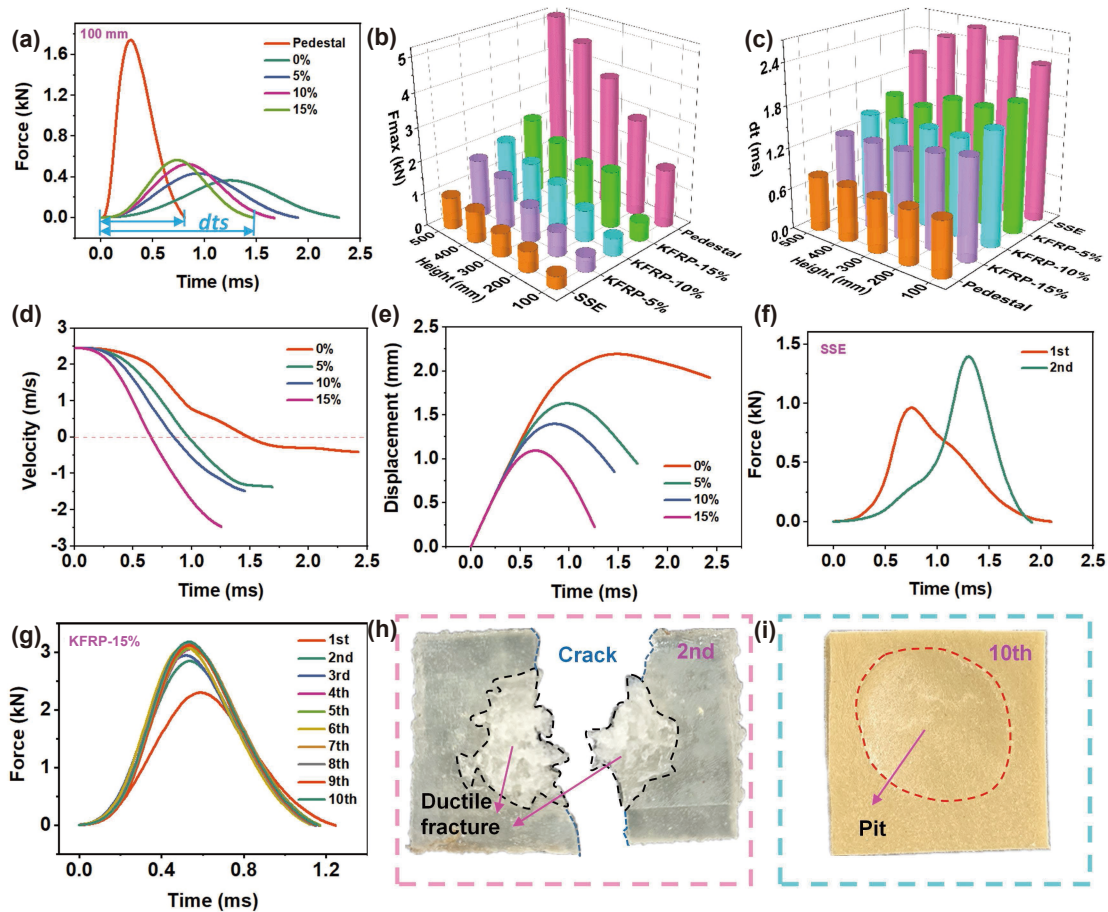
Fig. 3. (a) The impact forces vs. time of KFRPs loaded by drop hammer falling from 100 mm. Falling height dependent (b) impact force and (c) impact time. The (d) velocities and (e) displacements of the drop hammer during impact when the initial height was 300 mm. (f) The forces of SSE in two consecutive impacts. (g) The forces of KFRP-15% in ten repeated impacts. Morphologies of (h) SSE after twice impact and (i) KFRP-15% after tenth hit.

0.2 mm/s to 4 mm/s.

3.3 Anti-impact characteristics of KFRP under the drop hammer test

Furthermore, a drop hammer test was performed to investigate the anti-impact and energy-dissipation properties of KFRP. The drop hammer (0.55 kg) would fall from varying heights. The impact forces on the back of the composites (30 mm × 30 mm × 2.5 mm) were recorded. For instance, the maximum impact force (F_{max}) on the pedestal was 1.74 kN at a falling height of 100 mm (Fig. 3a). However, it remarkably decreased to 0.37 kN and 0.56 kN after dissipation by SSE and KFRP-15% respectively. In addition, the buffer times (*dts*) of KFRP were also much longer than those loaded directly on the pedestal, indicating an effective ability to dissipate impact energy. Additionally, the similar force responses under the impact from 200 mm to 500 mm are also shown in Fig. S6, and the F_{max} and *dts* are compared in Fig. 3b and c. There was an increment trend in F_{max} and a decrement trend in *dts* as the KF contents increased, showing a slight degradation in the energy-dissipation properties. Nevertheless, the F_{max} of KFRP-15% correspondingly dissipated by 67.6%, 41.2%, 59.3%, 58.9%, and 55.7% compared with direct impact from 100 mm to 500 mm. Similarly, the *dts* of KFRP-15% was extended by 81.4%, 73.9%, 62.0%, 58.8%, and 57.1%, revealing that KFRP-15% still possessed excellent en-

ergy absorption ability.

Additionally, photographs of KFRP after one hammer impact drop are shown in Fig. S7a. There was serious damage to the SSE but a small sag for the KFRP-15%. The damage caused by KFRP-15% was significantly alleviated, showing its ability to resist destruction was enhanced. In addition, the velocities and displacements of the drop hammer during the 300 mm impact process are presented in Fig. 3d and e. The hammer touched the KFRP at an initial speed of 2.45 m/s. The increase in KF contents of KFRP resulted in a faster decay of velocity to zero and a decrement in impact displacement. For example, when impacting SSE, the maximum displacement of the hammer reached 2.2 mm at 1.48 s, while it only used 0.65 s to 1.1 mm when hitting KFRP-15%. Consequently, the anti-impact property of KFRP-15% was higher than that of SSE.

Moreover, the mechanical stability of KFRP under repeated falling loadings from 500 mm was further studied. The forces of two consecutive impacts of SSE and those of ten repeated hits of KFRP-15% are recorded in Fig. 3f and g, respectively. The second F_{max} of SSE was 1.40 kN, which increased by 0.44 kN compared with the first impact. In particular, SSE was completely destroyed after two impacts (Fig. 3h). The failure occurred from the contact area with the hammer, which indicated that the internal stress of SSE caused by the second impact exceeded its strength limit, res-

ulting in large plastic deformation, cracks and fractures. On contrast, the F_{max} of KFRP-15% showed an increasing trend up to the fourth impact, and the saturation was approximately 3.1 kN thereafter. Meanwhile, KFRP-15% still kept the sample intact after the tenth impact and only formed a small groove (Fig. 3i). Furthermore, the times of impact before KFRP failure during the repeated drop hammer test are measured and shown in Fig. S7b. KFRP-15% was destroyed after 41 consecutive impacts, which was 39, 34, and 27 more than SSE, KFRP-5%, and KFRP-10%, respectively. This enhancing mechanical properties of KFRP could be attributed to the staggered distribution of fibers in the matrix, improving the overall stiffness of the material. Hence, KFRP-15% was more suitable to employ for protection materials.

3.4 Stab resistance performance of KFRP under knife and spike impact

Furthermore, static puncture experiments were conducted at a rate of 1 mm/s to investigate the stab resistance performance of KFRP. The spike and knife are shown in Fig. S8a. The spike acupuncture force-displacement curves of the KFRP are

presented in Fig. 4a. There was a significant positive correlation between penetration forces and KF contents. For instance, the force of SSE was 0.38 N when the impact displacement was 10 mm. The penetration forces of KFRP were 3.28 N, 4.79 N, and 6.87 N, respectively, corresponding to KF contents of 5%, 10%, and 15%. This result revealed that there was an 18-fold improvement in spike resistance for KFRP-15% compared with the neat SSE. Moreover, the forces of KFRP-15% under different puncture rates are shown in Fig. 4b. The acupuncture process could be divided into two parts. In the primary period, the spike was gradually inserted into the KFRP and the puncture diameter was continuously enlarged. Subsequently, the puncture diameter remained stable while the displacement continued to increase, during which the puncture force was mainly the friction between the spike and KFRP. Additionally, KFRP-15% exhibited a rate-dependent enhanced effect because of the shear stiffening behavior of the matrix. Similarly, knife cutting impeding forces for KFRP were also remarkably improved (Fig. 4c). As the mass fraction of KFs varied from 0% to 15%, the penetration
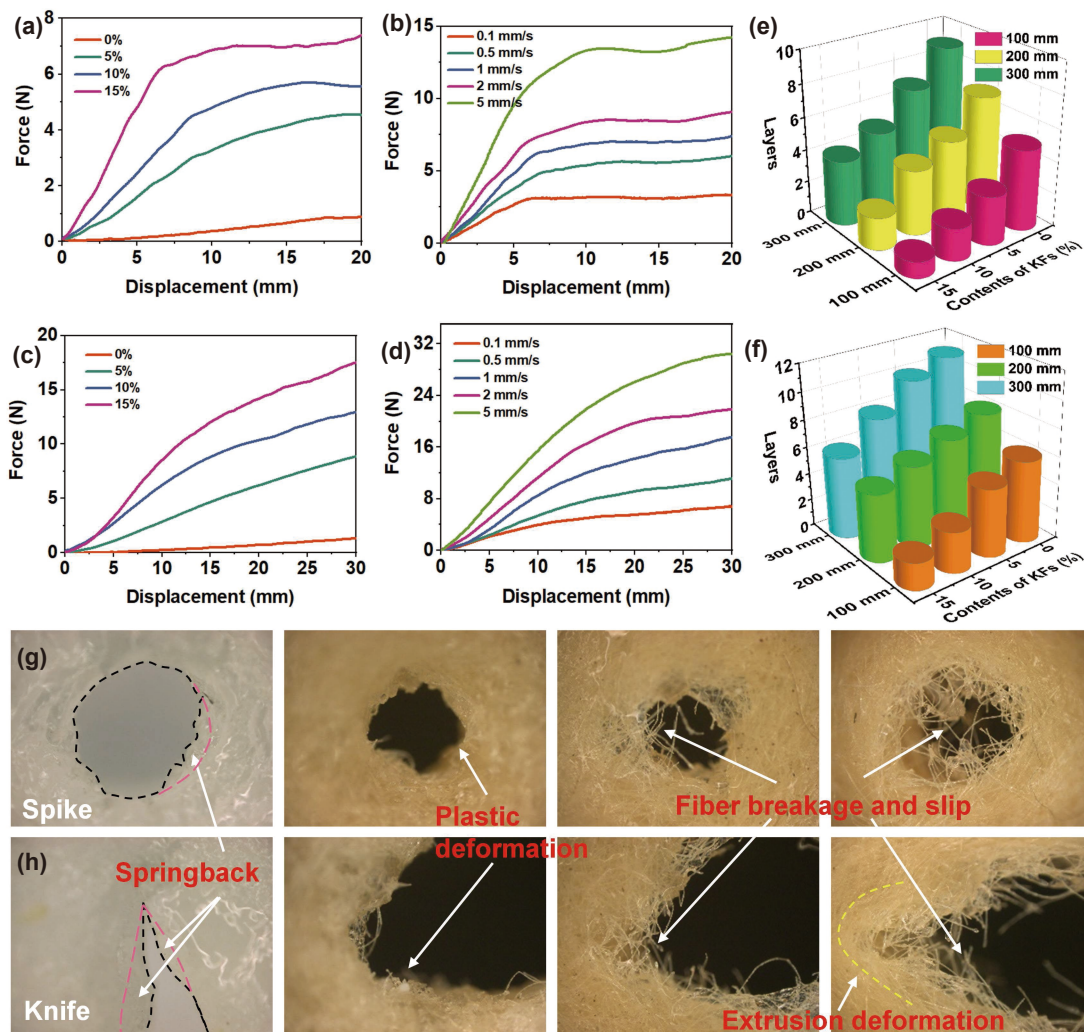

Fig. 4. The force-displacement curves of KFRP during (a) spike punch and (c) knife cutting at a rate of 1 mm/s. The force-displacement curves of 15%-KFRP at different (b) spike and (d) knife acupuncture speeds. The number of dynamic penetrating layers of KFRP when (e) spike and (f) knife puncturing. Microscopic photos of destruction topography: (g) spike punching and (h) knife cutting.

force increased from 1.32 N to 17.50 N at a displacement of 30 mm. In addition, the rate-enhanced knife mechanical performance is also illustrated in Fig. 4d. Accordingly, the higher mass fraction of KFs showed better stab resistance performance for the KFRP composites.

Moreover, the excellent stab resistance of KFRP against the spike and knife during dynamic drop impact is demonstrated in Fig. 4e and f, respectively. The test devices are shown in Fig. S8b and c. The KFRP targets were placed on the multi-layer foam backing (Fig. S8d), which consisted of a polyethylene sponge, witness paper, and base. The layer of penetrated witness papers corresponded to the penetration depth. Therefore, it could be used to evaluate the stab resistance of the target. The KFRP presented a lower penetration depth than the SSE under the same impact heights. The spike penetration depth of SSE at the height of 300 mm was 11 layers which was much higher than 6 layers of KFRP-15%. Besides, for KFRP-15%, the depth was 2 layers of witness papers when the knife cutting height was 200 mm, while the depth of SSE was 7 layers. Remarkably, the penetration depth of the witness papers decreased significantly with increasing KF weight ratios, which indicated that the stab resistance performance improved.

In addition, the damage morphologies of KFRP after spike punching and knife cutting were analyzed to explore the failure mechanisms (Fig. 4g and h). Plastic deformation of KFRP was observed while there was a spring back for SSE. This was attributed to the elasticity and softness of the SSE. compared with KFRP-10%, more fibers of KFRP-15% were damaged in the fracture section. Fibers were squeezed, slipped, and bent with the matrix, or even fractured during the impact- or contact with the KFRP[29]. The failure of KFRP under the stab resistance test was mainly due to the slippage of the KFs and matrix, slightly owing to the cutting-off of fibers. Therefore, KFRP-15% exhibited higher energy dissipation and larger impact force because of the increase in KFs.

3.5 Thermal properties of KFRP

Besides improving the mechanical performance of composite materials, KFs can also enhance their thermal properties. Therefore, it was essential to analyze the thermal properties of KFRP. From Fig. 5a–c and Table S2, the addition of KFs enhanced the thermal conductivities and thermal diffusivities but reduced the specific heat values. The thermal conductivity of KFRP-15% increased by 32.8%, and its thermal diffusivity increased from 0.126 mm²/s to 0.202 mm²/s compared with SSE. In contrast, the specific heat of KFRP-15% was the lowest. These were because the fact that KFs with high as-
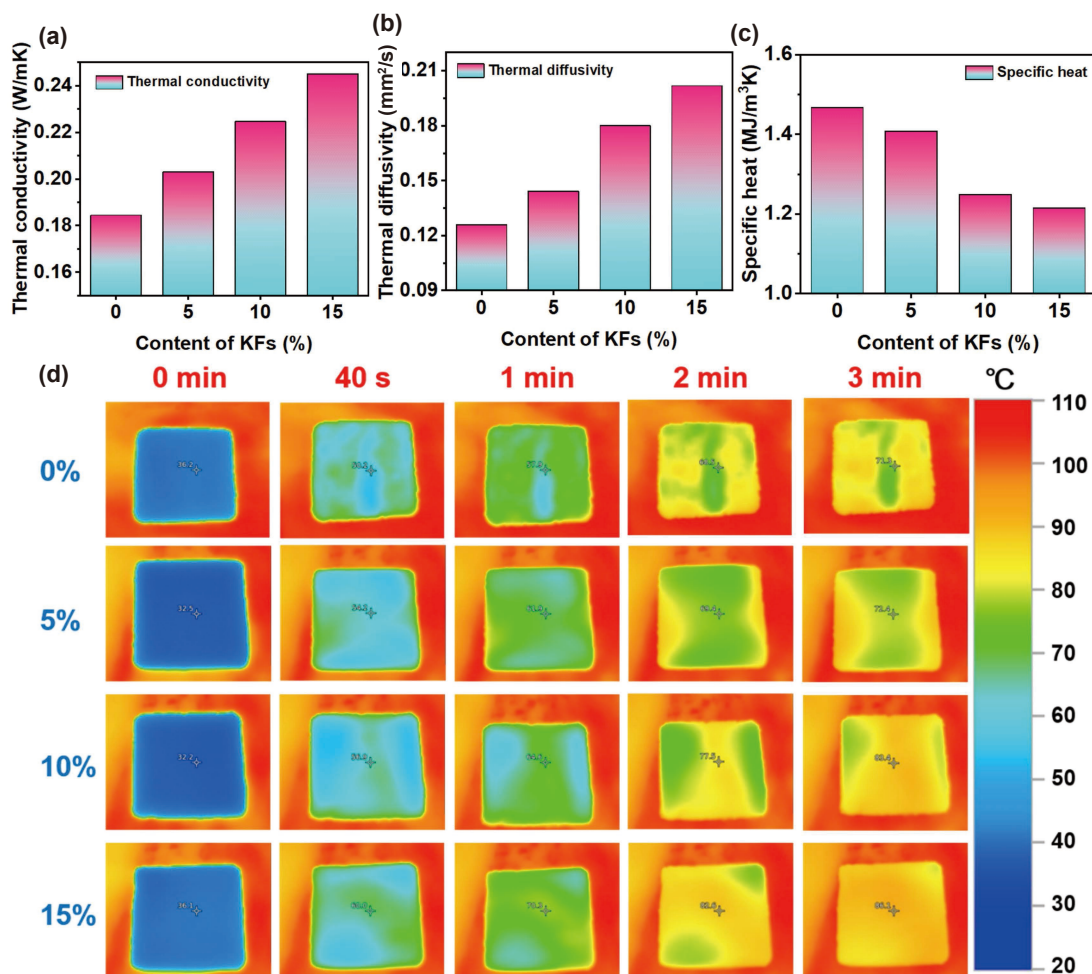

Fig. 5. (a) The thermal conductivity, (b) thermal diffusivity, and (c) specific heat of KFRP. (d) Infrared thermal images of the top surfaces of KFRP at different times from 0 min to 3 min.

pect ratios built thermally conductive paths in the SSE, which allowed heat to flow more efficiently through the material[30]. Furthermore, a visual method was developed to evaluate the heat transfer performance of KFRP at high temperatures. The 2-mm-thick composite was placed on a 100 ℃ heating stage. The dynamic temperature variation on the top surface was monitored by an infrared thermometer (Fig. 5d). Because of the relatively high thermal conductivity and thermal diffusivity of KFRP-15%, the temperature on the top surface increased quickly and faster became uniformly distributed. The surface infrared temperature of KFRP-15% reached 86.3 ℃ in 3 min, while the local temperature of SSE was only 71.3 ℃. As a result, SSE hybridized with KFs demonstrated good heat dissipation capacity.

Due to the excellent thermal stability and flame retardancy of KFs, it was necessary to investigate the combustion behavior of KFRP. The cone calorimetry test was performed to effectively evaluate the flame retardancy and smoke suppression of KFRP in a real fire (Fig. 6). The times to ignition of KFRP were prolonged as presented in Fig. 6a. The time to ignition of KFRP-15% was 38 s, which was an increase of 5 s compared to SSE. More importantly, the heat release rate (HRR) and total heat release (THR) results are illustrated in Fig. 6b and c, respectively. It was noteworthy that the peak HRRs (PHRRs) of KFRP were approximately 300 kW/m^2, which dramatically declined from that of pure SSE (405.6 kW/m^2). Besides, before the burning time of 750 s, the THRs of KFRP with 5%, 10% and 15% KFs were all less than SSE. Furthermore, the smoke production properties of KFRP were measured. With the increase in KFs, the smoke production rate (SPR) of KFRP effectively declined (Fig. 6d). At 100 s, the SPR of KFRP-15% was 0.05 mm^2/s, which was 45% of SSE. As observed in Fig. 6e, the maximum total smoke production (TSP) of pure SSE was 19.1 m^2. The maximum TSPs of KFRP-10% and KFRP-15% were decreased by 15.7% and 22.0%, respectively. These results proved that the addition of KFs to SSE could effectively inhibit the release of smoke and dust during combustion. The mass loss curves of pure SSE and KFRP are shown in (Fig. 6f). The mass of pure SSE was

reduced quickly after ignition. Subsequently, the combustion ended at approximately 460 s, and there was 24% residue remained. In particular, the mass loss rates of KFRP decreased, and their char residues increased. Consequently, KFRP-15% exhibited better flame retardant and smoke suppression effects than SSE.

3.6 Functional bracers based on KFRP-15%

Accordingly, the bracers based on KFRP-15% for protection, thermal dissipation, and flame-retardance were fabricated. In addition, expandable polyethylene (EPE), commonly used for buffering, protection, and packaging, was served for contrast (Fig. 7a). First, the impact energy dissipation performance of KFRP-15% and EPE under heavy hammer impact was studied (Fig. S9a). KFRP-15% exhibited better protection than EPE, and the F_{max} is compared in Fig. S9b. For example, the F_{max} on the pedestal and EPE was 5.20 kN and 4.73 kN at a falling height of 500 mm, respectively. However, it remarkably decreased to 2.30 kN after dissipation by KFRP-15%. Furthermore, KFRP-15% could block falling sharp knife, while EPE was pierced (Fig. 7b and Movie S1). Additionally, due to the excellent heat transfer performance, the KFRP-15% based wristband could dissipate the body temperature faster than EPE (Fig. 7c). Finally, the EPE-based bracer was flammable and could burn violently after being exposed to the flame for 2.5 s (Fig. 7d). However, the bracer based on KFRP-15% undoubtedly showed better fire-resistant properties, which were not ignited by the flame for more than 10 s (Movie S2). Photos of KFRP-15% and EPE after burning are presented in Fig. S9c.

4   Conclusions

In summary, advanced functional safeguarding composites were developed by dispersing short KFs into SSE, which presented ameliorative mechanical, heat-transfer, and flame retardant performance. KFRP-15% exhibited a typical shear stiffening behavior. Additionally, the vertical tensile strength
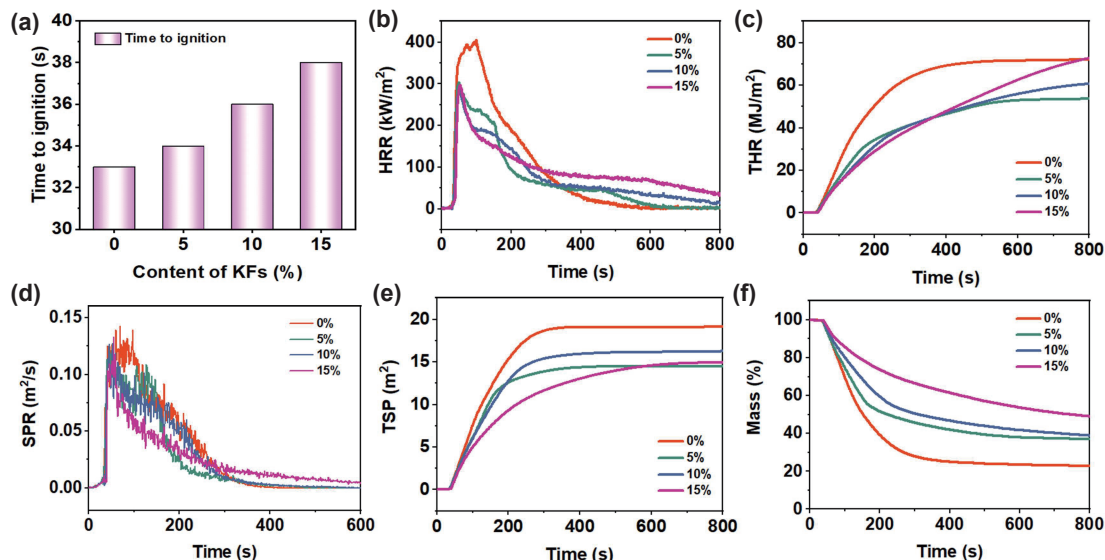

Fig. 6. (a) Time to ignition, (b) HRR, (c) THR, (d) SPR, (e) TSP, and (f) mass loss of KFRP.

Fig. 7. (a) Photographs of the bracers based on KFRP-15% and EPE. (b) Infrared thermal images of bracers. (c) The process of the sharp knife impacting KFRP-15% and EPE in free fall. (d) Burning photos of the bracers based on KFRP-15% and EPE.

of KFRP-15% increased from 0.12 MPa to 2.62 MPa compared with SSE. The fracture toughness of vertical KFRP-15% was enhanced by 2243.1% compared with that of SSE. KFRP-15% could effectively limit the propagation of the crack tip, demonstrating better tear resistance than SSE. Moreover, the maximum hammer impact force and buffer time of KFRP-15% were correspondingly dissipated by 67.6% and extended by 81.4% compared to direct impact from 100 mm, indicating its excellent energy absorption ability. Meanwhile, KFRP-15% presented significant stab resistance performance under impact by spike and knife. Furthermore, the thermal conductivity, flame retardancy, and smoke suppression capabilities of KFRP-15% were improved due to the introduction of KFs. All these enhancements were attributed to the robust and thermally stable features of Kevlar fibers combined with their staggered and layered dispersion in the SSE matrix. Ultimately, a multi-functional KFRP-15%-based bracer was developed, which exhibited superior performance in protection, heat transfer and flame retardance. Thus, this work provides an effective way to prepare high-performance fiber-enhanced polymer composites that show promise for application in the security field.

Supporting information

The supporting information for this article can be found online at https://doi.org/10.52396/JUSTC-2022-0089. The supporting information includes nine figures, two tables, and two movies.

Acknowledgements

Conflict of interest

The authors declare that they have no conflict of interest.

Biographies

Wenhui Wang received her Bachelor degree from China University of Petroleum (East China). She is currently a Ph.D. candidate under the supervision of Prof. Xinglong Gong in the Intelligent Materials and Vibration Control Laboratory at the University of Science and Technology of China. Her research focuses on shear thickening materials and smart anti-impact devices.

Sheng Wang received his Ph.D. degree from University of Science and Technology of China (USTC) in 2017. Then, he was a postdoctoral fellow in the CAS Key Laboratory of Mechanical Behavior and Design of Materials in Hefei. Now he is an Associate Professor at USTC. His research interests include smart materials and devices with magnetic, electric, and force-sensing properties. He is also interested in developing multifunctional triboelectric nanogenerator systems.

Xinglong Gong received his Ph.D. degree in Mechanics from both the University of Science and Technology of China (USTC) and Saitama University in 1996. Then, he worked at the Nihon Dempa Kogyo Co., Ltd., Japan. In 2003, he joined the Department of Modern Mechanics, USTC, as a Full Professor. He is currently the Chief Editor of Chinese Journal of Experimental Mechanics, Director of CAS Key Laboratory of Mechanical Behavior and Design of Materials. His research interests comprise soft matter materials as well as their applications. He was supported by the 100-Talent Programme of Chinese Academy of Sciences in 2003 and supported by the National Science Foundation for Distinguished Young Scholars of China in 2011.

References

[1] Nayak R, Crouch I, Kanesalingam S, et al. Body armor for stab and spike protection, Part 1: Scientific literature review. *Textile Research Journal,* **2018**, *88* (7): 812–832.

[2] Lou L, Chen K, Fan J. Advanced materials for personal thermal and moisture management of health care workers wearing PPE. *Materials Science and Engineering: R: Reports,* **2021**, *146*: 100639.

[3] Liu X, Shao Q, Cao J, et al. Superamphiphobic and flame-resistant cotton fabrics for protective clothing. *Cellulose,* **2022**, *29*: 619–632.

[4] Feng Y, He C, Wen Y et al. Multi-functional interface tailoring for enhancing thermal conductivity, flame retardancy and dynamic mechanical property of epoxy/Al_2O_3 composites. *Composites Science and Technology,* **2018**, *160*: 42–49.

[5] Zhao X, Copenhaver K, Wang L, et al. Recycling of natural fiber composites: Challenges and opportunities. *Resources, Conservation and Recycling,* **2022**, *177*: 105962.

[6] Ye Y Y, Liang S D, Feng P, et al. Recyclable LRS FRP composites for engineering structures: Current status and future opportunities. *Composites Part B: Engineering,* **2021**, *212*: 108689.

[7] Polyzos E, Van Hemelrijck D, Pyl L. Numerical modelling of the elastic properties of 3D-printed specimens of thermoplastic matrix reinforced with continuous fibres. *Composites Part B: Engineering,* **2021**, *211*: 108671.

[8] Naveen J, Jawaid M, Zainudin E S, et al. Thermal degradation and viscoelastic properties of Kevlar/*Cocos nucifera* sheath reinforced epoxy hybrid composites. *Composite Structures,* **2019**, *219*: 194–202.

[9] Wang W, Zhou J, Wang S, et al. Enhanced Kevlar-based triboelectric nanogenerator with anti-impact and sensing performance towards wireless alarm system. *Nano Energy,* **2022**, *91*: 106657.

[10] Wang H, Wang H, Wang Y, et al. Laser writing of Janus graphene/Kevlar textile for intelligent protective clothing. *ACS Nano,* **2020**, *14* (3): 3219–3226.

[11] Sun W, Zhang J, Xie M, et al. Ultrathin aramid/COF heterolayered membrane for solid-state Li-metal batteries. *Nano Letters,* **2020**, *20*: 8120–8126.

[12] Fu S, Yu B, Tang W, et al. Mechanical properties of polypropylene composites reinforced by hydrolyzed and microfibrillated Kevlar fibers. *Composites Science and Technology,* **2018**, *163*: 141–150.

[13] Chen Y, Yin Q, Zhang X, et al. Rational design of multifunctional properties for styrene-butadiene rubber reinforced by modified Kevlar nanofibers. *Composites Part B: Engineering,* **2019**, *166*: 196–203.

[14] Yuan F, Salpekar D, Baburaj A, et al. Fiber-reinforced monolithic supercapacitors with interdigitated interfaces. *Journal of Materials Chemistry A,* **2021**, *9*: 11033–11041.

[15] Lyu J, Liu Z, Wu X, et al. Nanofibrous Kevlar aerogel films and their phase-change composites for highly efficient infrared stealth. *ACS Nano,* **2019**, *13* (2): 2236–2245.

[16] Zheng L, Zhang K, Liu L, et al. Biomimetic architectured Kevlar/polyimide composites with ultra-light, superior anti-compressive and flame-retardant properties. *Composites Part B: Engineering,* **2022**, *230*: 109485.

[17] Lu W, Yu W, Zhang B, et al. Kevlar fibers reinforced straw wastes-polyethylene composites: Combining toughness, strength and self-extinguishing capabilities. *Composites Part B: Engineering,* **2021**, *223*: 109117.

[18] Yuan F, Wang S, Zhang S, et al. A flexible viscoelastic coupling cable with self-adapted electrical properties and anti-impact performance toward shapeable electronic devices. *Journal of Materials Chemistry C,* **2019**, *7*: 8412–8422.

[19] Yuan F, Liu S, Zhou J, et al. Smart touchless triboelectric nanogenerator towards safeguard and 3D morphological awareness. *Nano Energy,* **2021**, *86*: 106071.

[20] Ding L, Zhang S, Wang Q, et al. Self-healing and printable elastomer with excellent shear stiffening and magnetorheological properties. *Composites Science and Technology,* **2022**, *223*: 109430.

[21] Zhang S, Wang S, Zheng Y, et al. Coaxial 3D-Printed and kirigami-inspired deployable wearable electronics for complex body surfaces. *Composites Science and Technology,* **2021**, *216*: 109041.

[22] Sang M, Zhang J, Liu S, et al. Advanced MXene/shear stiffening composite-based sensor with high-performance electromagnetic interference shielding and anti-impacting bi-protection properties for smart wearable device. *Chemical Engineering Journal,* **2022**, *440*: 135869.

[23] Wang S, Ding L, Wang Y et al. Multifunctional triboelectric nanogenerator towards impact energy harvesting and safeguards. *Nano Energy,* **2019**, *59*: 434–442.

[24] Wang Y, Gao Y, Liu Y, et al. Optimal aperture and digital speckle optimization in digital image correlation. *Experimental Mechanics,* **2021**, *61*: 677–684.

[25] Su Y, Gao Z, Tu H, et al. Uniformity and isotropy of speckle pattern cause the doubled random error phenomenon in digital image correlation. *Optics and Lasers in Engineering,* **2020**, *131*: 106097.

[26] Zhao A, Shi X Y, Sun S H, et al. Insights into the Payne effect of carbon black filled styrene-butadiene rubber compounds. *Chinese Journal of Polymer Science,* **2021**, *39*: 81–90.

[27] Xu H, Fan X, Song Y, et al. Reinforcement and Payne effect of hydrophobic silica filled natural rubber nanocomposites. *Composites Science and Technology,* **2020**, *187*: 107943.

[28] Binti Yusoff R, Takagi H, Nakagaito A N. Tensile and flexural properties of polylactic acid-based hybrid green composites reinforced by kenaf, bamboo and coir fibers. *Industrial Crops and Products,* **2016**, *94*: 562–573.

[29] Kim H, Kim G, Lee S, et al. Strain rate effects on the compressive and tensile behavior of bundle-type polyamide fiber-reinforced cementitious composites. *Composites Part B: Engineering,* **2019**, *160*: 50–65.

[30] Han Y, Shi X, Wang S, et al. Nest-like hetero-structured BNNS@SiCnws fillers and significant improvement on thermal conductivities of epoxy composites. *Composites Part B: Engineering,* **2021**, *210*: 108666.